Journal of Materials Chemistry A

Remaking the chlor-alkali electrolysis process to co-generate useful reduction products from CO2

Journal:	*Journal of Materials Chemistry A*
Manuscript ID	TA-ART-05-2023-003202.R1
Article Type:	Paper
Date Submitted by the Author:	07-Aug-2023
Complete List of Authors:	Li, Yifei; Rutgers The State University of New Jersey, Chemistry and Chemical Biology Laursen, Anders ; RenewCO2, LLC Dhiman, Mahak ; Rutgers University, Department of Chemistry and Chemical Biology Dismukes, Gerard; Rutgers University, Chemistry & Chemical Biology

ARTICLE

Remaking the chlor-alkali electrolysis process to co-generate useful reduction products from CO_2

Received 00th January 20xx,
Accepted 00th January 20xx

DOI: 10.1039/x0xx00000x

Yifei Li,[a] Anders Laursen,[a, b] Mahak Dhiman[a] and G. Charles Dismukes *[a, c]

Converting CO_2 into usable chemicals and fuels electrochemically is a promising method to close the carbon cycle and store intermittent renewable energy. However, combining it with the typical anode, the oxygen evolution reaction (OER), results in both high energy consumption and produces only oxygen of little commercial value. Conversely, the chlor-alkali process is an established and profitable electrochemical process that produces Cl_2 and alkali (KOH). Herein, we demonstrate the feasibility of integrating the chlorine evolution reaction (CER) together with CO_2 reduction reactions (CO_2RR) to co-generate C_4 (2,3-furandiol) and C_3 (methylglyoxal) products. At a cell current of 1mA, the system produces Cl_2 with Faradaic efficiency (FE) of ~80% and CO_2RR at 100% without losses from crossover or degradation of the cathode. High Faradaic efficiency is achieved for CO_2RR products at higher current densities using nickel phosphide Ni_2P catalyst synthesized by a low temperature soft-template method. A technoeconomic assessment is presented that quantifies the economic advantage of combining the co-production of methylglyoxal and Cl_2 by integrating these two electrochemical processes.

Introduction

Reducing both energy consumption and resource waste is a priority for green and sustainable development of chemical industries. The switch from thermochemical to low temperature electrosynthesis methods offers advantages for both metrics[1]. Electrochemical manufacturing of bulk chemicals has a long history but is limited in the range of products to mainly inorganic feedstocks. Herein, we examine both the technical challenges and the economics of electrosynthesis of CO_2 reduction products as possible replacement for the chlor-alkali cathode reaction.

The chlor-alkali (CA) process is one such energy intensive electrolysis process that produces chlorine (Cl_2), sodium hydroxide (NaOH) and hydrogen (H_2) from salt brine (NaCl)[2] . An alternative chlor-alkali process that uses O_2 at the cathode is more energy efficient but without forming H_2[3]. The economic viability of all aqueous electrolysis processes depends on the highly variable cost of electricity and competition with the expanding hydrogen markets[4]. Techno-economic modelling of chlor-alkali processes indicates that flexibility using a combination of these two cathodes or a bifunctional cathode for operational mode switching on short timescales along with demand side management of production could be a future solution[5]. These economic factors have motivated consideration of alternative cathode products of higher economic value that are needed at comparable scales.

Chlorine (Cl_2) is one of the largest scale manufactured chemicals due to its many uses in plastics, solvents, chemicals and as oxidants. Chlorine is produced via electrolysis of rock salt (NaCl) or hydrochloric acid (HCl) by an energy intensive process. At present, there are three variations on the chlor-alkali process, with the most widely adopted and economical one being the The Bayer-Uhdenora process using an oxygen-depolarized electrode and operating at a cell potential of E_o^{cell}-0.96 V[6]. Alternatively, the Bayer-Uhde-Hoechst electrolysis process produces H_2 at the cathode but has higher electricity cost arising from the greater cell potential, E_o^{cell}-2.16 V. There are no commercially demonstrated alternative cathode reactions for the chlor-alkali process to our knowledge.

Experimental and computational studies have examined combining Cl_2 production with CO_2 reduction reactions (CO_2RR) to simple C_1 gaseous products like carbon monoxide (CO) or syngas (H_2 + CO)[7]. Li et al. demonstrated the potential of electrolytically producing phosgene gas from CO and Cl_2.[8] However, syngas is a comparatively low value product compared to some C_2 and C_{2+} products which can be used to synthesize more valuable longer-chain hydrocarbons and oxygenates. Liquid products require alternative, more costly separation strategies.

Significant progress has been made in recent years in developing electrocatalysts for selective CO_2RR to multi-carbon products[9-16]. Using copper supported on gas-diffusion electrodes with PTFE, 50% of the current produces multicarbon products (ethylene, ethanol and 1-propanol), while the other

[a] Department of chemistry and chemical biology, 123 Bevier Rd, Piscataway, NJ 08854
[b] RenewCO$_2$ Inc.,418 Orchard Street Cranford, Piscataway, NJ 07016-1745,
[c] Waksman Institute of technology, 190 Frelinghuysen Rd, Piscataway, NJ.
Electronic Supplementary Information (ESI) available: See DOI: 10.1039/x0xs0000x

half makes H_2[17]. The overall electrical energy conversion efficiency for an electrochemical process is the product of the current conversion efficiency (here 50%) times the cell voltage efficiency. For the noted example, at the operating cell voltage of 4.2 V the overall electrical to synthetic fuel energy conversion efficiency to C_2 and C_3 products (ethylene and propanol) is 19%, which is 5-10-fold better than ethanol biofuel.

Transition metal phosphides contain multifunctional sites that can break the linear scaling relationship of simple metal catalysts[18]. For example, among the nickel phosphides (Ni_xP_y) five different crystalline phases were shown to produce three oxyhydrocarbons products (C_1, C_3 and C_4), with the best catalysts achieving current conversion efficiencies (Faradaic) above 99%[19, 20]. Among these, Ni_2P showed the highest Faradaic efficiency (71%) toward 2,3-furandiol (C_4) at 10 mV overpotential, while NiP_2 produced methylglyoxal (C_3) at 83% efficiency [21]. The mechanisms of formation of these C_3 and C_4 products involve complex 12-electron and 14-electron processes that are significantly slower than the competing H_2 evolution reaction[21]. The scale of the methylglyoxal global market was $1.36 million in 2018 and continues to grow at an annual rate of 7.9% [22-25]. In addition, it has been reported that methylglyoxal can replace formaldehyde as a cross-linking agent in polymers[26], and as an additive to diesel blends used as fuel to reduce the CO_2 emissions[27]. The potential market size of methylglyoxal is calculated to be $108 billion when including the markets of formaldehyde and 10% of diesel[28, 29].

In order to design a commercially competitive process to make multi-carbon liquid products from CO_2 at bulk scale, most studies have focused on cathode catalysts, while little attention has been paid to compatibility with the anode reaction[30].

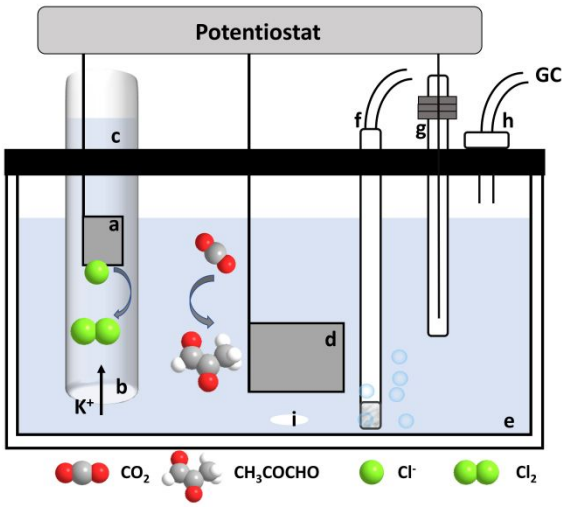

Fig. 1 Schematic drawing of the electrochemical H-cell utilized to produce methylglyoxal and chlorine gas:(a) dimensionally stabilized anode; (b) Nafion membrane; (c) The anode compartment, in which saturated KCl solution was used as anolyte; (d) Ni_2P as cathode; (e) cathode compartment, in which 0.5M $KHCO_3$ is used as catholyte; (f) CO_2 inlet; (g) reference electrode; (h) CO_2 outlet; (i) stir bar

Generally, CO_2RR is coupled with the water oxidation/oxygen evolution (OER), a kinetically irreversible four-electron process that exhibits a substantial overpotential on most electrodes[31-33]. Alternatively, substituting the OER with alcohol oxidation reaction (AOR) at the anode can lower the cell voltage, however, the current density decreases compared to the standard CO_2RR/OER combination.[34] Other challenges of AOR include (1) poor reaction selectivity because AOR can go through multiple different pathways at adequate current densities; (2) anodic catalyst degradation from the organics that poison the electrocatalysts.[34, 35] By contrast, chloride oxidation is a simple reversible one-electron/Cl^- ion process on most metal catalysts[36-38]. Herein, we investigate the compatibility of these reactions in terms of the reaction kinetics and thermodynamic constraints that control the product yield over selected environmental conditions applicable to the chlor-alkali process. A preliminary techno-economic analysis based upon our experimental results and literature data is also provided that suggests this overall process could be economically competitive.

Experimental Section

2.1 Electrochemical measurements

A schematic of the three-electrode electrochemical glass cell (Gamry Instruments) is summarized in **Fig. 1**. It is equipped with 5 ports: one for CO_2 gas inlet; one for gas outlet to the GC; one each for the reference and working electrodes; and one port for the separate anode compartment comprised of an electrode, electrolyte and membrane. A stir bar is used below the working electrode to suppress bubble accumulation. A proton conducting membrane (Nafion 117, Fuel Cell Store) is used to connect the catholyte and anolyte compartments, while preventing convective mixing and slowing the diffusive crossover of methyl glyoxal and Cl_2 gas. The catholyte is 0.5 M aqueous $KHCO_3$ treated with Chelex 100 (molecular biology grade resin). Before the reaction, the electrolyte was purged with CO_2 (Airgas, instrument grade, with a Supelco hydrocarbon trap) to ensure a CO_2-saturated solution, a continuous flow of gas at 5 sccm was kept during the reaction as regulated by a mass flow controller. Saturated KCl solution (pH=2 adjusted with HCl) was utilized as the anolyte. Additional KCl crystals were added to the solution to ensure saturation during the reaction.

The reference electrode is $Hg/Hg_2SO_4/K_2SO_4$, which is calibrated daily against an Accumet standard calomel electrode (SCE). A commercial dimensionally stabilized anode (DSA, DeNora) with an area of ~0.073 cm^2 was utilized as a counter electrode. It is comprised of RuO_2/TiO_2 supported on Ti mesh, which matches the commercial electrode design[39]. To prepare the cathode, 200 mg Ni_2P with 50 µL Nafion (Sigma Aldrich 5 wt% solution in lower aliphatic alcohols and water) were ground, and the mixture was pressed into a pellet at 4 ton/cm^2 for 2 min by analogy to previous experiments[21]. Electrolysis was performed with a Biologics potentiostat. The Ohmic drop between the working and the reference electrodes was measured and

compensated by the electrochemical workstation. The electrode potential recorded in the experiment is given by the formula: E(RHE) = E(SCE) + 0.0591 pH + 0.2715.

2.2 Catalyst Synthesis and characterization

We adopted a detergent templating procedure to increase the surface area of the Ni_2P catalyst compared to the standard solid-state synthesis[40]. Firstly, cetyltrimethylammonium bromide (CTAB) and sodium mono-dodecyl phosphate were stirred (700 RPM) in 200 mL solution of water and cyclohexane (ratio: 1:1) for 15 mins at room temperature. Then 10mL 1-hexanol was added into the mixture dropwise and the mixture was further stirred for 30 mins. Nickel chloride hexahydrate salt (10 g) and red phosphorous (12 g) were added into the solution. After the mixture was transferred into a Teflon-sealed autoclave reactor, it was heated to 195 °C for 24 h. The black solid product (Ni_2P) formed was isolated by centrifugation by washing with water three times. The isolated Ni_2P was further washed with 3% HCl to remove the surface phosphate/ oxide species, followed by ethanol wash. The as-synthesized materials were dried at 60 °C for 6 h.

SEM/EDX mapping was done using a Zeiss Sigma Field Emission Scanning Electron Microscope (FESEM) equipped with an Oxford X-Max EDS detector and Oxford Nordlys EBSD detector. Powder X-ray diffraction was performed at room temperature on a Philips Xpert powder diffractometer, spinning at 100 rpm, Cu K-alpha 0.15418 nm, calibrated daily with a Si standard.

2.3 Product Detection and Faradic Efficiency Measurements

The volatile gas products were analyzed by Gas Chromatograph (GC; SRI model 8610C). Here, the headspace of the cell was directly connected to the GC for online analysis. The apparatus was purged before reaction to check for air leakage, and then every 1 hour during the measurements. The liquid products were detected and quantified by an offline high-performance liquid chromatography (HPLC; Perkin Elmers Flexer) with an autosampler, UV-vis detector and refractive index detector (RID). Product assignment was established by retention time of HPLC and confirmed by 1H NMR (chemical shifts and splitting multiplicity), as described in detail in the ESI and in Calvinho et al.[21]. The product yield of Cl_2 was measured by iodometric titration using **Equations (1) and (2)**[7].

$$Cl_2 + 2I^- \leftrightarrow 2Cl^- + I_2 \quad (1)$$

$$I_2 + 2S_2O_3^{2-} \leftrightarrow S_4O_6^{2-} + 2I^- \quad (2)$$

Results and Discussion

Techno-economic estimation. Dhiman et al. reported electrosynthesis of methylglyoxal at a faradaic efficiency up to 47% at a total current density ranging from 50 to 300 mA/cm^2 using single-phase Ni_2P catalyst prepared as ultra-high surface area morphology and applied to a gas diffusion electrode.[40] These design criteria and use of a flow cell eliminated the fall-off of CO_2RR yield to H_2 even at this upper current density. Here, we use their performance data to do an initial techno-economic feasibility (TEF) of an integrated system combining electroreduction of CO_2 to methylglyoxal (at 50% FE) and chloride oxidation to Cl_2 (at 100% FE). The costs are categorized into capital costs (CAPEX) and operating costs (OPEX). All calculations are shown in Supporting Information. The capital costs include the electrolyzer, balance of plant (10% of the electrolyzer cost) and the downstream purification cost (0.6 million $) for methylglyoxal, which includes purification distillation, rectifier column, stripping column, molecular sieve, heat exchanger, product tank, and pump. The electrolyzer is the main cost at $32 million for a 50,000 kg/day MEG capacity plant, based on a $423/kW electrolyzer cost (uninstalled).[41] This is a conservative estimate based on recent TEF evaluations of CO_2RR at scale[42]. The plant lifetime is conservatively estimated to be 20 years, though it is typically longer for chlor-alkali plants. The operating cost are based on estimates that include the current cost of electricity ($0.056/kWh)[43], maintenance (3% OPEX/year), the cost of raw materials (CO_2, H_2O, KCl) and the cost of purification of the delivered Cl_2 product, which totals $0.442 million/day. Our TEF assessment provides a daily profit of $1.53 million/day (324% of the daily OPEX + daily amortized CAPEX). Therefore, the proposed integrated system is commercially attractive even with the current cost of electricity.

Synthesis. The SEM image in **Fig. 2a** shows the morphology of Ni_2P synthesized by the soft-templating method. It produces a sponge-like morphology consisting of porous sheets several microns in dimension and with holes of diameter ranging from 50 to 200 nm distributed uniformly with no obvious aggregation. The surface/volume ratio of Ni_2P prepared by this method[40] is approximately 260-fold greater than obtained using the high temperature solid-state synthesis method [21]. Powder X-ray diffraction measurements (**Fig. 2b**) reveal that all diffraction peaks matched well with the crystal structure of Ni_2P (ICDD # 01-074-1385). Assignment of all peaks is given in the SI. There are no extraneous peaks from secondary phases, nor low theta features from amorphous material. This synthesis method creates a pure product in a single crystal phase.

Selectivity between OER and CER. The oxygen evolution reaction (OER) is the main competing reaction for chloride electrolysis. It needs to be minimized due to its safety risk and degradation of the CER catalyst[44]. The overall reaction stoichiometries and standard electrochemical potentials are given in **Equations (3) and (4)**:

$$2H_2O \rightarrow O_2 + 4H^+ + 4e^-$$
$$E^o_{\frac{O2}{H2O}} = (1.229 - 0.059\,\mathrm{p}H)\ V\ vs\ SHE \quad (3)$$

$$2Cl^- \rightarrow Cl_2 + 2e^-$$
$$E^o_{\frac{Cl2}{Cl^-}} = 1.358V\ vs\ SHE \quad (4)$$

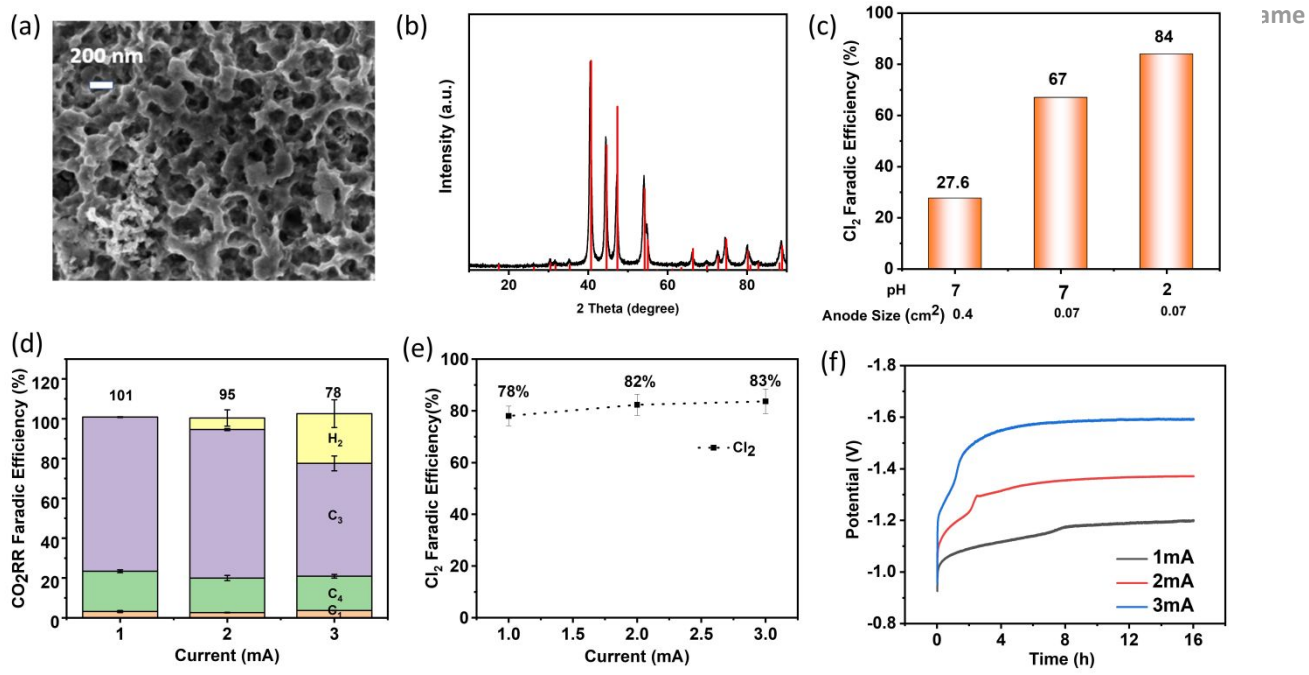

Fig. 2 (a) Typical SEM image of Ni_2P nanosheets. (b) XRD pattern of the synthesized Ni_2P nanosheets. (c) Faradaic efficiency for CER at different current densities and pH. The remaining product is O_2. Anode compartment is saturated KCl (pH ~2 adjusted with HCl). Cathode compartment is 0.5 M $KHCO_3$ bubbled with CO_2 (saturated); (d)(e) Faradaic efficiency for CO_2RR and CER, respectively, as a function of current after removal of the surface oxide by electroreduction. N= 3 replicates; (f) Representative chronopotentiometry measurements at different potentials for Ni_2P. Due to the high porosity of the catalyst, there is an initial charging period for reduction of surface oxide after which the potential stabilizes.

Although the cell potential for the Cl_2/Cl^- couple ($E°$ = 1.36 V vs NHE) is 130 mV higher than $E°$ for the O_2/H_2O couple (1.23 V), the Cl_2 evolution reaction (CER) is mechanistically simpler ($1e^-/Cl^-$, zero H^+) vs the complex OER (concerted $4e^-/O_2$, plus $4H^+$)[45, 46]. This complexity can be exploited kinetically or energetically to favour CER. For example, the simpler $2e^-$ reaction pathway ($2H_2O \rightarrow H_2O_2 \rightarrow O_2$) still requires two water molecules (e.g., must be concerted) and has a higher energy barrier to the peroxide intermediate with $E°$ (H_2O_2/H_2O) = 1.776 V. The non-concerted one-electron pathway forms hydroxyl radicals from individual water molecules and has an even higher energy barrier with $E°(OH^-/H_2O)$ = 2.75 eV. Therefore, CER can be selected over OER in four ways: 1) It is favoured energetically at low applied overpotentials; 2) It is kinetically favored as it requires one Cl^-/e^-; 3) It does not take up or consume protons and this is favoured at low pH **(Equations 3 and 4)**; 4) Because Cl^- anions are electrostatically concentrated at the positive anode vs uncharged water molecules, CER is favoured in low ionic strength electrolytes and at higher applied potential.

Accordingly, we examined increasing the anode charge density by limiting the area of the anode at higher current densities. We used a commercial dimensionally stabilized anode (DSA) comprised of TiO_2-RuO_2-IrO_2, which has been shown to be an efficient catalyst for CER[16, 39, 47, 48]. **Fig. 2c** shows chronopotentiometry experiments using anode sizes of 0.4 cm^2 and 0.07 cm^2. The measured FE for Cl_2 at pH 7 increases from 27% to 67%, respectively, as predicted.

Next, we adjusted the pH of the anode compartment from neutral to pH~2 by using HCl to investigate suppression of the OER. The FE for Cl_2 production increased further to 84% (**Fig. 2e**). Subsequent electrolysis experiments were conducted at pH~2 since under this condition, there was no observable corrosion of the anode by the electrolyte over the course of all experiments.[45] Cl_2 disproportionate in water/alkali to form hypochlorite, $OCl^- + Cl^- + 2H^+$, which occurs above pH 3[49]. Similar conditions are used for the industrial production of Cl_2 to avoid substantial losses from the OER side reaction[50].

During electrolysis, the catholyte pH increases from its initial value of 7.5 as OH^- is co-generated during the reduction of both water and CO_2. As a result, bicarbonate will form which can cause an added complexity to long-term operation, yet $KHCO_3$ is also a profitable product, as shown in the TEF evaluation given in the ESI. In addition, the by-product $KHCO_3$ can be easily separated by precipitation in a practical flow cell system[7]. The cell reaction that occurs at the anode and cathode and the net cell equations are as follows:

$$Cathode: 3CO_2 + 12\,(e^- + H^+) \rightarrow C_3H_4O_2 + 2H_2O \quad (5)$$

$$Acid - base\ reaction: CO_2 + OH^- \rightarrow HCO_3^- \quad (6)$$

$$Anode\ reaction: 2Cl^- - 2e^- \rightarrow Cl_2 \quad (7)$$

$$Total\ equation:$$

$$15CO_2 + 8H_2O + 12Cl^- \rightarrow C_3H_4O_2 + 6Cl_2 + 12HCO_3^- \quad (8)$$

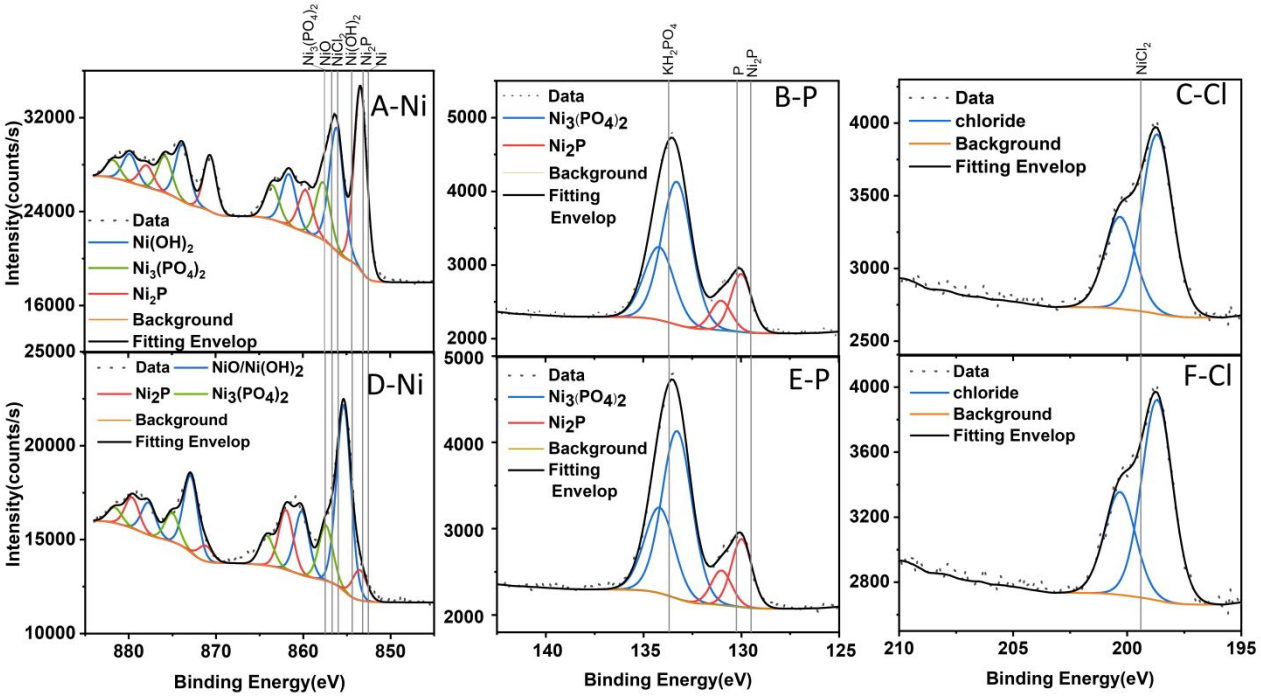

Fig. 3 XPS spectra of the Ni_2P cathode before and after electrolysis (from left) Ni 2p (A and D), and P 2p (B and E) and Cl 2p (C and F) with fitted spectra. The top row is the pristine cathode prior to exposure to electrolyte; the bottom row is the catalytically cycled cathode.

Combining CO_2RR and CER. Chronopotentiometry was used to measure the integrated currents (**Fig. 2f**) at three different values and integrate the charge passed to account for all cathode and anode products as individual Faradaic efficiencies (**Fig. 2d**). These data were collected at currents of 1, 2 and 3 mA over 4 hours of operation, corresponding to the cathode currents densities normalized to geometric area of ~0.8, 1.6 and 2.5 mA/cm^2, respectively. During electrolysis, the headspace of the cell was connected to an online GC for gas analysis. The only gaseous product formed during electrolysis was H_2. The liquid products were identified by HPLC retention time and ^{1}H-NMR (chemical shifts and spin multiplicities) to be formic acid, 2,3-furandiol and methylglyoxal. The total measured FE for all CO_2RR products is 100% at 1 mA, 96% at 2 mA and 78% at 3 mA. The measured FE for the HER is 0%, 4% and 22%, respectively. At 0.8 mA/cm^2 the maximum selectivity is for methylglyoxal at 78%, with 2,3-furandiol the second major product, in agreement with a prior report using the identical catalyst and surface area[40]. Although formic acid is produced at all potentials, its Faradaic efficiency never exceeds 5% for any of the three currents. **Table 1**[21] lists the standard electrochemical potentials for each product, which shows that the 12-electron C_3 and 14-electron C_4 products are thermodynamically favoured relative to HER. However, the facile kinetics of HER outcompetes CO_2RR at increasing current densities. To separate the methylglyoxal from the mixture, distillation might be feasible considering the different boiling points of methylglyoxal (73 °C), formic acid (100.7 °C) and 2,3-furandiol (211.9 °C). We included an estimated cost for distillation in the TEF.

Table 1 Standard electrochemical potentials at pH 7.0[21]

Product	Half Reaction	$E^{o'}$(V vs RHE)
Hydrogen	$2(e^- + H^+) \leftrightarrow H_2$	0.00
Formic acid	$CO_2 + 2(e^- + H^+) \leftrightarrow HCOOH$	-0.02
Methylglyoxal	$3CO_2 + 12(e^- + H^+) \leftrightarrow C_3H_4O_2 + 4H_2O$	+0.02
2,3-furandiol	$4CO_2 + 14(e^- + H^+) \leftrightarrow C_4H_4O_3 + 5H_2O$	+0.01

To understand why these products form, consider that five nickel phosphide binary compounds (Ni_xP_y) all convert CO_2 into the same C_1, C_3 and C_4 products by an identical mechanism that is distinct from copper-based catalysts. Calvinho et al.[21] proposed an 11-step mechanism that has been supported by additional experimental[20,40] and computational[20,51] evidence. The potential determining step is CO_2 insertion into a surface hydride bond to form an adsorbed formate species, *$HCOO^-$. This intermediate can either dissociate or be attacked by another *hydride and protonated to form formaldehyde H_2CO* and water. H_2CO* undergoes two consecutive exergonic self-condensation reactions to form *glyceraldehyde followed by an exergonic dehydration reaction which yields methylglyoxal as a main product. The *methylglyoxal precursor undergoes endergonic keto-enol tautomerism, which permits another exoergic aldol condensation with H_2CO* to form a *C_4 aldol intermediate. This intermediate can then cyclize by an exergonic intramolecular *aldol reaction, before a final exergonic *dehydrogenation to form 2,3-furandiol. All evidence to date supports this mechanism, including: (1) the time and temperature dependence of the three products; (2) replacing CO_2 with any of the three products yields the same products; (3) adding CO slows the rate of CO_2RR (inhibits the above mechanism)[20] and (4) density functional theory calculations by

Rappe et al.[51] which further confirmed this mechanism. Other transition metal phosphides also show similar product selectivity: copper phosphides convert CO_2 into formate[52]; iron phosphides generates 2,3-furandiol, methylglyoxal, formate and ethylene glycol from CO_2 which is explained by the above mechanism[20]. For CO_2RR on Fe_2P, both Grand Canonical-DFT calculations and experimental results demonstrate that *formate is the crucial intermediate that forms from surface phosphino-hydrides in contrast to *CO intermediate on copper-based catalysts.

To determine the amount of Cl_2 produced during the 4-hour electrolysis, 5 mL of anolyte was removed from the cell and titrated after each 2-hour of electrolysis. This volume was replaced with 5 mL of fresh electrolyte in the anode compartment. We measured the Faradaic efficiency of CER by collecting the anolyte with acidified potassium iodide solution. **Fig. 2e** shows the Faradaic efficiency of Cl_2 production increases smoothly from 78% to 82% between 1 and 3 mA. Triplicate results at two current densities are 79 ± 3% and 81 ± 3% for 50 mA cm^{-2} and 75 mA cm^{-2} j_{total}, respectively. O_2 accounts for the remaining product as shown in the SI.

We measured the stability of the Ni_2P catalyst during co-production of Cl_2 by chronopotentiometry over 16 hours. The data given in **Fig. 2f** shows that the potential decreases in the first half hour of the experiment due to the reduction of the surface phosphates to phosphides and nickel oxides to water, in agreement with the previous CO_2RR study on Ni_2P coupling with OER[21, 40]. After the initial break-in period, the potential stabilizes, and nearly constant potential is observed, indicating that CER does not adversely affect the stability of CO_2RR on Ni_2P. The maximum Cl_2 faradic efficiency in the anode compartment at the end of the 16 h period was measured to be 78% Faradaic efficiency. As noted, this value increases at higher current densities. Linear sweep voltammetry was conducted to evaluate the performance of Ni_2P in the condition of CO_2-saturated 0 .5 M $KHCO_3$ (red lines) and in Ar-saturated 0.25 M $Na_4P_2O_7$ (black lines) as shown in **Fig. S2**. At more negative potentials, the latter showed higher current density, indicating CO_2 has occupied the HER active sites leading to lower current density. However, at the potentials higher than -0.2 V, red trace showed a higher current density, indicting the high activity of CO_2RR.

Surfaces changes following catalysis. A concern in combining CER with CO_2RR is the possible crossover of Cl_2 from anode to cathode compartments, and its potential negative effect on the catalyst activity and stability and CO_2RR product yields. We observed no diminution in total CO_2RR yield or distribution relative to experiments using an OER catalyst at the anode and the same Ni_2P catalyst at the cathode[40]. To gain further information about the surface of Ni_2P we used X-ray photoelectron spectroscopy (XPS) to analyze the elemental composition and speciation. The experimental and fitted XPS spectra of the 2p core levels of Ni, P and Cl are presented in **Fig. 3** for the Ni_2P catalyst.

The Ni 2p spectra are shown in **Fig. 3**. The Ni $2p_{3/2}$ and Ni $2p_{1/2}$ doublet has average splitting ~20 eV and arises from the atomic spin-orbital coupling. Each of these regions can be fit to six resolved gaussian transitions of different widths by a least-squares fitting algorithm, as shown. The peaks are shifted by their respective chemical environments. Our assignments of chemical speciation are based on previous studies[18, 21, 53-55]. The Ni $2p_{3/2}$ part of the spectrum reveals three main peaks (852.4–854.4 eV, 854.4–857.2 eV, 857.2- 858.9 eV) along with their corresponding satellite peaks at approximately 6.0 eV higher than that of the Ni^{2+} species. We assign these to reduced $Ni^{\delta+}$ species in the Ni_2P phase, Ni^{2+} ions from nickel hydroxide and/or oxide ($Ni(OH)_2$/NiO), and Ni^{2+} from $Ni_3(PO_4)_2$, respectively The hydroxide/oxide and phosphate species are assigned to functional groups on the surface of nickel phosphides as these peaks decrease upon reductive bias[56, 57]. The Ni 2p binding energy in the bulk material is higher than reported values for zero valence state Ni (852.4 eV) and lower than that of Ni in NiO (855.8 eV). This indicates partial transfer of electron density from Ni to P, yielding a partial positive charge (δ+), where $0 < \delta < 2$[53, 54, 58].

Comparing the Ni 2p spectra before and after electrolysis, it is noted that the intensity ratio decreases between the $Ni^{\delta+}$ peak from Ni_2P to the Ni^{2+} peaks from $Ni(OH)_2$/NiO and $Ni_3(PO_4)_2$, indicating a higher degree of surface oxidation after exposure to the electrolyte compared to the as-synthesized catalyst in air[21].

Inspection of the P 2p spectra in **Fig. 3B and E** reveals two resolved peaks that fit to two pairs of gaussians. The unresolved splitting arises from the $2p_{3/2}$ and $2p_{1/2}$ spin-orbit splitting regions that are fitted to two gaussian peaks. The first peak centered at 129.9 eV can be assigned to reduced $P^{\delta-}$ from Ni_2P, the second peak at 133.3 eV can be assigned to oxidized phosphorus at a similar transition as $Ni_3(PO_4)$. These assignments are consistent with the Ni spectra. Based on the positions in relation to the database, we note that the P species in Ni_2P carries a small negative charge ($P^{\delta-}$), where $0<\delta<1$, since the values of the P 2p binding energies are less than the reported value of elemental phosphorus (130.2 eV)[53, 54, 58]. As shown in **Fig. 3E**, the ratio of $P^{\delta-}/PO_4^{3-}$ decreases significantly after catalytic turnover and exposure to electrolyte in air, in agreement with the previous results showing that nickel phosphides hydrolyze upon exposure to electrolyte in air.

As shown in **Fig. 3C and F**, the characteristic $2p_{3/2}$ and $2p_{1/2}$ peaks of chlorine were detected on the cathode both before and after electrolysis. There was no change in intensity or line shape, indicating that only trace environmental chlorine is present and no accumulation occurs following electrolysis for 16 hours corresponding to 57.6 coulombs passed. This is further confirmed by the similar atomic percentage calculated through the Cl 2p peak averaged by three different samples before and after catalysis: 1.49 ± 0.65 % and 1.40 ± 1.03 %, respectively. The peak at 198.7 eV is attributed to residual chloride during

the catalyst synthesis procedure, which binds with Ni_2P chemically as shown in **Fig. S7**. By comparing catalysts with and without acid washing, we found that Cl remains, as shown in below **Fig. S7a**. The atomic percentage is 1.34 ± 0.47 %, similar to the Ni_2P catalyst without acid washing (1.49 ± 0.65 %). This shows that the Cl originates from the nickel chloride used in the synthesis procedure and is not mainly coming from the HCl washing. By further washing the catalyst repeatedly for 10 times with distilled water, the Cl remains, as shown in **Fig. S7b**, indicating that the residual Cl binds strongly within the nickel phosphide. We conclude that the significant yield of Cl_2 produced during the electrolysis in the anode compartment (> 78% Faradaic efficiency) does not accumulate on the cathode, nor does it modify the CO_2RR product yield based on the measured Faradaic efficiencies.

Conclusions

A combined electrolysis system modelled on the chlor-alkali process was tested for the first time to convert CO_2 to liquid products (C_4>C_3>C_1) on Ni_2P and chloride to chlorine. Under an applied voltage of -0.079 V vs RHE (1 mA), the system produces Cl_2 with Faradaic efficiency ~80% and CO_2RR products at ~100% (no H_2). At higher applied potentials (higher current density) the Cl_2 Faradaic efficiency improves in competition with less O_2 evolution, while H_2 evolution increases (20% FE) in competition with CO_2RR products (80% FE) at 0.48 V vs RHE (3 mA). The absence of Faradaic losses from Cl_2 crossover and the unobservable interference with the Ni_2P electrode bodes well for future scale up of this configuration. The system demonstrates the techno-economic advantage of combining co-production of Cl_2 with high CO_2 conversion to predominantly a single C_3 product (methylglyoxal) that could serve as an environmental-friendly alternative for petrochemically derived C_3 feedstocks.

Author Contributions

GCD proposed the research direction. GCD, ABL and YL designed and planned the experiments. YL performed the experiments. Catalyst preparation and characterization were performed by MD. GCD and YL wrote the manuscript with inputs from ABL. All authors read and approved the manuscript.

Conflicts of interest

There are no conflicts to declare.

Acknowledgements

This research has been funded by the DOE-SBIR program under a subcontract to RenewCO_2 LLC. Contract number 828028.

Notes and references

1. L.-N. Zhang, R. Li, H.-Y. Zang, H.-Q. Tan, Z.-H. Kang, Y.-H. Wang and Y.-G. Li, *Energy & Environmental Science*, 2021, **14**, 6191-6210.
2. J. Crook and A. Mousavi, *Environmental Forensics*, 2016, **17**, 211-217.
3. K. Li, Q. Fan, H. Chuai, H. Liu, S. Zhang and X. Ma, *Transactions of Tianjin University*, 2021, **27**, 202-216.
4. L. C. Brée, K. Perrey, A. Bulan and A. Mitsos, *AIChE Journal*, 2018, **65**.
5. L. C. Brée, A. Bulan, R. Herding, J. Kuhlmann, A. Mitsos, K. Perrey and K. Roh, *Industrial & Engineering Chemistry Research*, 2020, **59**, 12186-12196.
6. J. Pérez-Ramírez, C. Mondelli, T. Schmidt, O. F. K. Schlüter, A. Wolf, L. Mleczko and T. Dreier, *Energy & Environmental Science*, 2011, **4**.
7. J.-H. Guo and W.-Y. Sun, *Applied Catalysis B: Environmental*, 2020, **275**.
8. C. Li, J. Shi, J. Liu, Y. Duan, Y. Hua, S. Wu, J. Zhang, X. Zhang, B. Yang and Y. Dai, *Electrochimica Acta*, 2021, **389**.
9. H. Xu, D. Rebollar, H. He, L. Chong, Y. Liu, C. Liu, C.-J. Sun, T. Li, J. V. Muntean, R. E. Winans, D.-J. Liu and T. Xu, *Nature Energy*, 2020, **5**, 623-632.
10. Y. Xue, Y. Guo, H. Cui and Z. Zhou, *Small Methods*, 2021, **5**, e2100736.
11. B. Yang, K. Liu, H. Li, C. Liu, J. Fu, H. Li, J. E. Huang, P. Ou, T. Alkayyali, C. Cai, Y. Duan, H. Liu, P. An, N. Zhang, W. Li, X. Qiu, C. Jia, J. Hu, L. Chai, Z. Lin, Y. Gao, M. Miyauchi, E. Cortes, S. A. Maier and M. Liu, *J Am Chem Soc*, 2022, **144**, 3039-3049.
12. B. Zhang, J. Zhang, M. Hua, Q. Wan, Z. Su, X. Tan, L. Liu, F. Zhang, G. Chen, D. Tan, X. Cheng, B. Han, L. Zheng and G. Mo, *J Am Chem Soc*, 2020, **142**, 13606-13613.
13. F. P. G. d. Arquer, C.-T. Dinh, A. Ozden, J. Wicks, C. McCallum, A. R. Kirmani, D.-H. Nam, C. Gabardo, A. Seifitokaldani, X. Wang, Y. C. Li, F. Li, J. Edwards, L. J. Richter, S. J. Thorpe, D. Sinton and E. H. Sargent, *Science*, 2020, **367**, 661-666.
14. M. G. Kibria, C. T. Dinh, A. Seifitokaldani, P. De Luna, T. Burdyny, R. Quintero-Bermudez, M. B. Ross, O. S. Bushuyev, F. P. Garcia de Arquer, P. Yang, D. Sinton and E. H. Sargent, 2018, **30**, e1804867.
15. W. Ma, S. Xie, T. Liu, Q. Fan, J. Ye, F. Sun, Z. Jiang, Q. Zhang, J. Cheng and Y. Wang, *Nature Catalysis*, 2020, DOI: 10.1038/s41929-020-0450-0.
16. Y. Zhou, F. Che, M. Liu, C. Zou, Z. Liang, P. De Luna, H. Yuan, J. Li, Z. Wang, H. Xie, H. Li, P. Chen, E. Bladt, R. Quintero-Bermudez, T. K. Sham, S. Bals, J. Hofkens, D. Sinton, G. Chen and E. H. Sargent, *Nat Chem*, 2018, **10**, 974-980.
17. J. E. Huang, F. Li, A. Ozden, A. S. Rasouli, F. P. G. d. Arquer, S. Liu, S. Zhang, M. Luo, X. Wang, Y. Lum, Y. Xu, K. Bertens, R. K. Miao, C.-T. Dinh, D. Sinton and E. H. Sargent, *Science*, 2021, **372**, 1074-1078.
18. A. T. Landers, M. Fields, D. A. Torelli, J. Xiao, T. R. Hellstern, S. A. Francis, C. Tsai, J. Kibsgaard, N. S. Lewis, K. Chan, C. Hahn and T. F. Jaramillo, *ACS Energy Letters*, 2018, **3**, 1450-1457.
19. L. Ji, L. Li, X. Ji, Y. Zhang, S. Mou, T. Wu, Q. Liu, B. Li, X. Zhu, Y. Luo, X. Shi, A. M. Asiri and X. Sun, *Angew Chem Int Ed Engl*, 2020, **59**, 758-762.
20. K. U. D. Calvinho, A. W. Alherz, K. M. K. Yap, A. B. Laursen, S. Hwang, Z. J. L. Bare, Z. Clifford, C. B. Musgrave and G. C. Dismukes, *J Am Chem Soc*, 2021, **143**, 21275-21285.
21. K. U. D. Calvinho, A. B. Laursen, K. M. K. Yap, T. A. Goetjen, S. Hwang, N. Murali, B. Mejia-Sosa, A. Lubarski, K. M. Teeluck, E. S.

Hall, E. Garfunkel, M. Greenblatt and G. C. Dismukes, *Energy & Environmental Science*, 2018, **11**, 2550-2559.
22. S. Sankaralingam, A. Ibrahim, M. M. D. Rahman, H. A. Eid and S. Munusamy, *Current Pharmaceutical Design*, 2018, **24**, 3072-3083.
23. I. Nemet, L. Varga-Defterdarovic and Z. Turk, *Mol Nutr Food Res*, 2006, **50**, 1105-1117.
24. R. Ramasamy, S. F. Yan and A. M. Schmidt, *Cell*, 2006, **124**, 258-260.
25. Methylglyoxal (CAS 78-98-8) Market Research Report, https://dataintelo.com/report/global-methylglyoxal-%28cas-78-98-8%29-market/).
26. W. Henning Althofer and M. Robert Loos, *United States Patent*, 2010, **US 2011/0124807 A1**.
27. S. Voelker, S. Deutz, J. Burre, D. Bongartz, A. Omari, B. Lehrheuer, A. Mitsos, S. Pischinger, A. Bardow and N. von der Assen, *Sustainable Energy & Fuels*, 2022, **6**, 1959-1973.
28. Formaldehyde market size and market growth opportunities, https://www.einnews.com/pr_news/595296687/global-formaldehyde-market-size-and-market-growth-opportunities#:~:text=LONDON%2C%20GREATER%20LONDON%2C%20UK%2C,(CAGR)%20of%206.5%25Global).
29. Diesel Engine Market: Global Industry Trends, Share, Size, Growth, Opportunity and Forecast 2023-2028, https://www.imarcgroup.com/diesel-engine-market).
30. M. Jouny, W. Luc and F. Jiao, *Industrial & Engineering Chemistry Research*, 2018, **57**, 2165-2177.
31. E. Fabbri and T. J. Schmidt, *Acs Catal*, 2018, **8**, 9765-9774.
32. T. Naito, T. Shinagawa, T. Nishimoto and K. Takanabe, *Inorganic Chemistry Frontiers*, 2021, **8**, 2900-2917.
33. X. Xie, L. Du, L. Yan, S. Park, Y. Qiu, J. Sokolowski, W. Wang and Y. Shao, *Advanced Functional Materials*, 2022, **32**.
34. A. Vass, A. Kormanyos, Z. Koszo, B. Endrodi and C. Janaky, *Acs Catal*, 2022, **12**, 1037-1051.
35. X. Zhao, L. Du, B. You and Y. Sun, *Catal Sci Technol*, 2020, **10**, 2711-2720.
36. H. Dong, W. Yu and M. R. Hoffmann, *The Journal of Physical Chemistry C*, 2021, **125**, 20745-20761.
37. J. S. Ko, J. K. Johnson, P. I. Johnson and Z. Xia, *ChemCatChem*, 2020, **12**, 4526-4532.
38. D. Y. Kuo, H. Paik, J. N. Nelson, K. M. Shen, D. G. Schlom and J. Suntivich, *J Chem Phys*, 2019, **150**, 041726.
39. S. Trasatti, *Electrochimica Acta*, 2000, **45**, 2377-2385.
40. M. Dhiman, Y. Chen, Y. Li, A. B. Laursen, K. U. D. Calvinho, T. G. Deutsch and G. C. Dismukes, *Journal of Materials Chemistry A*, 2023, DOI: 10.1039/d2ta08173c.
41. B. James, W. Colella and J. Moton, *PEM Electrolysis H2A Production Case Study Documentation*, 2013.
42. P. De Luna, C. Hahn, D. Higgins, S. A. Jaffer, T. F. Jaramillo and E. H. Sargent, *Science*, 2019, **364**.
43. Energy Prices Data Explorer, IEA, https://www.iea.org/data-and-statistics/data-tools/energy-prices-data-explorer).
44. A. R. Zeradjanin, N. Menzel, W. Schuhmann and P. Strasser, *Phys Chem Chem Phys*, 2014, **16**, 13741-13747.
45. J. G. Vos, Z. Liu, F. D. Speck, N. Perini, W. Fu, S. Cherevko and M. T. M. Koper, *Acs Catal*, 2019, **9**, 8561-8574.
46. J. Du, Z. Chen, C. Chen and T. J. Meyer, *J Am Chem Soc*, 2015, **137**, 3193-3196.
47. D. Dionisio, L. H. E. Santos, M. A. Rodrigo and A. J. Motheo, *Electrochimica Acta*, 2020, **338**.
48. C. E. Finke, S. T. Omelchenko, J. T. Jasper, M. F. Lichterman, C. G. Read, N. S. Lewis and M. R. Hoffmann, *Energy Environ Sci*, 2019, **12**, 358-365.
49. R. K. Karlsson and A. Cornell, *Chem Rev*, 2016, **116**, 2982-3028.
50. T. E. Lister and E. J. Dufek, *Energy & Fuels*, 2013, **27**, 4244-4249.
51. S. Banerjee, A. Kakekhani, R. B. Wexler and A. M. Rappe, *Acs Catal*, 2021, **11**, 11706-11715.
52. A. B. Laursen, K. U. D. Calvinho, T. A. Goetjen, K. M. K. Yap, S. Hwang, H. Yang, E. Garfunkel and G. C. Dismukes, *Electrochimica Acta*, 2021, **391**.
53. G. Yun, Q. Guan and W. Li, *Rsc Adv*, 2017, **7**, 8677-8687.
54. Y. Pan, Y. Liu, J. Zhao, K. Yang, J. Liang, D. Liu, W. Hu, D. Liu, Y. Liu and C. Liu, *Journal of Materials Chemistry A*, 2015, **3**, 1656-1665.
55. L. I. Y. Luis J. Matienzo, Samuel O. Grim, and William E. Swartz, Jr., *Inorganic Chemistry*, 1973, **12**.
56. A. B. Laursen, Patraju, K.R., Whitaker, M.J., Retuerto, M., Sarkar, T., Yao, N., Ramanujachary, K.V., Greenblatt, M., Dismukes, G.C., *Energy & Environmental Science*, 2015, DOI: 10.1039/c4ee02940b.
57. A. B. Laursen, R. B. Wexler, M. J. Whitaker, E. J. Izett, K. U. D. Calvinho, S. Hwang, R. Rucker, H. Wang, J. Ji, E. Garfunkel, M. Greenblatt, A. M. Rappe and G. C. Dismukes, *Acs Catal*, 2018, **8**, 4408-4419.
58. A. K.-V. A. V. Naumkin, S. W. Gaarenstroom and C. J.Powel, accessed 1 January 2017.